Strong coherent ion-electron coupling using a wire data bus

Baiyi Yu, Ralf Betzholz, and Jianming Cai[*]

School of Physics, Hubei Key Laboratory of Gravitation and Quantum Physics, International Joint Laboratory on Quantum Sensing and Quantum Metrology, Institute for Quantum Science and Engineering, Huazhong University of Science and Technology, Wuhan 430074, China

Ion-ion coupling over long distances represents a highly useful resource for quantum technologies, for example, to sympathetically cool or interconnect qubits in ion-based quantum computing architectures. In this respect, the recently demonstrated wire-mediated ion-ion coupling stands due to the simplification of its trap layout and its prospects for deterministic entanglement. However, the strength of such coherent ion-wire-ion coupling is typically weak, hindering its practical utilization. Here, we propose a wire-mediated scheme for coherent ion-electron coupling. The scheme not only enables the sympathetic cooling of electrons via advanced ion-cooling techniques, but also allows promotion of the effective ion-ion coupling strength by orders of magnitudes via electron mediation. Our work thus paves a way toward quantum information processing in ion-electron hybrid quantum systems.

I. INTRODUCTION

Coherent coupling represents a paramount ingredient for the implementation of most quantum technologies [1–6], because it is crucial for establishing one of their most essential resources, namely the entanglement of different quantum mechanical degrees of freedom. For example, the coupling between qubits is an integral ingredient for the realization of entangling gates in quantum computing [7–14]. On the other hand, besides the coupling of different degrees of freedom within the same system, the coherent coupling of entirely different types of quantum systems is likewise intriguing, since it opens routes to build hybrid platforms, potentially harnessing and combining the advantages of different quantum systems [15–28].

Trapped-ion systems, with their rich internal energy levels, for instance, were shown to exhibit unique advantages in quantum information processing [29–42] and precision sensing [43–48], whereas trapped-electron systems, with their simpler spin-up and -down internal states, have a long history in high-precision measurements [49–57] and hold the potential to accelerate quantum information processing speed due to their remarkably large charge-to-mass ratio, as compared to ions [58–71]. Therefore, coherently coupling trapped ions and electrons could not only make established techniques based on lasers, such as laser cooling [72], indirectly applicable to trapped electrons, but could also substantially enhance the ion-ion coupling strength if their interaction is mediated by electrons.

However, this task is not straightforwardly achievable due to the extreme mass difference and opposite electric charges of ions and electrons. These differences pose a great challenge for trapping electrons and ions in close proximity in order to exploit the direct Coulomb interaction between them. Even in the scenario of a wire-mediated coupling [73], where electrons and ions are separately trapped and connected via a conductor wire, the typically large detuning between their motional frequencies significantly suppresses their interaction.

In this work, we propose a scheme to establish such a wire-mediated coherent coupling between trapped ions and electrons that remedies their frequency detuning through a local parametric modulation of the electron-trapping potential. Because of the remarkably greater charge-to-mass ratio of the electron, in feasible experimental setups, the wire-mediated ion-electron coupling strength for single particles could be orders of magnitude larger than the wire-mediated ion-ion coupling strength [73]. Building on this basic hybridization, we further discuss an electron-mediated ion-ion coupling scheme, which not only promises a faster generation of entanglement, but would also allow sympathetic [74–77] and even exchange cooling [78,79]. This, in turn, could promote precision measurements of charged particles, such as protons or antiprotons [80–86].

II. ION-ELECTRON COUPLING SCHEME

We consider a setup, schematically depicted in Fig. 1(a), for the coherent coupling of ions and electrons, that are separately trapped at two distant positions and connected

---

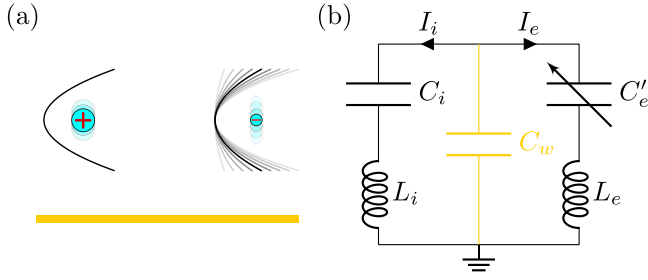[*]Contact author: jianmingcai@hust.edu.cn

(a)

(b)

FIG. 1. (a) Schematic of separately trapped ions and electrons connected via a conductor wire (golden line). The trapping potential of electron is properly modulated to ensure an effective coupling. (b) Equivalent circuit of the system shown in (a). The ion motion is equivalent to the LC circuit with capacitance C_i and inductance L_i, whereas the electron motion is equivalent to that with variable capacitance C_e' and inductance L_e. The conductor wire with capacitance C_w to the ground serves as a bridge between the two LC circuits.

via a conductor wire (represented in golden). The key problem that needs to be addressed is the large motional-frequency mismatch between the ions and the electrons for typical trapping potentials. This mismatch significantly suppresses the ion-electron coupling via the conductor wire. To overcome this difficulty, we implement a proper electric driving field in the axial direction of the electron trap, as indicated by the potential modulation (gray) in Fig. 1(a). This modulation results in an axial electron-motion component resonant with the axial ion motion, thereby effectively coupling the ions and electrons through a wire data bus despite the large mass difference between them. For the case of each trap holding a single particle, the axial-motion Hamiltonian of the combined ion-wire-electron system can be written as

$$H = H_i + H_e + H_I, \tag{1}$$

where $H_{i(e)}$ is the Hamiltonian of the axial ion (electron) motion and H_I describes the wire-mediated ion-electron coupling. Although Eq. (1) describes only the axial motion, the results remain valid when considering the full equation of motion for both Paul and Penning traps [43,87–89].

A. Hamiltonian and equivalent circuit

We then derive the explicit form of the Hamiltonian for the case of each trap holding a single particle following Ref. [90] and references therein. Firstly, we consider a fictitious situation where the conductor wire is at potential U_w and carries a total charge $Q_w = C_w U_w$, while the ion and the electron in each trap carry no charge. The effective distance $D_{i(e)}$ of the ion (electron) to the wire can be defined as

$$D_{i(e)} = \frac{U_w}{E_{i(e)}}, \tag{2}$$

where $E_{i(e)}$ is the electric field generated by the wire at the equilibrium position of the ion (electron) along the axial direction [73,76]. Then, the potential generated by the conductor wire at the ion (electron) position is given by

$$U_{i(e)} = U_{i(e),0} - x_{i(e)} \frac{U_w}{D_{i(e)}}, \tag{3}$$

where $x_{i(e)}$ is the position of the ion (electron) relative to its equilibrium point and $U_{i(e),0}$ is the potential generated by the conductor wire at the equilibrium point. One can then change to a dual case, where the wire has zero net charge and is at potential U_w', while the ion (electron) carries the charge $q_{i(e)}$. Application of Green's reciprocity theorem to these two cases leads to

$$U_w' = \frac{U_i q_i + U_e q_e}{Q_w}. \tag{4}$$

Combining this with Eq. (2), we can directly obtain the force exerted on the ion (electron) by the wire with potential U_w', namely,

$$F_{i(e)} = \frac{q_{i(e)} U_w'}{D_{i(e)}}. \tag{5}$$

Substituting Eqs. (3) and (4) into Eq. (5) and ignoring constant forces, we arrive at

$$F_i = -x_i \frac{q_i^2}{C_w D_i^2} - x_e \frac{q_i q_e}{C_w D_i D_e}, \tag{6}$$

$$F_e = -x_i \frac{q_i q_e}{C_w D_i D_e} - x_e \frac{q_e^2}{C_w D_e^2}. \tag{7}$$

We then take into account the trapping potentials of the ion and the electron and obtain

$$m_i \ddot{x}_i + m_i \omega_i^2 x_i - F_i = 0, \tag{8}$$

$$m_e \ddot{x}_e + m_e \omega_e^2 [1 + \eta \cos(\omega_d t)] x_e - F_e = 0, \tag{9}$$

where $m_{i(e)}$ and $\omega_{i(e)}$ represent the mass and harmonic trapping frequency of the ion (electron), respectively, whereas η and ω_d denote the depth and frequency of the driving field applied to the trapped electron, respectively. Substituting F_i and F_e with the expressions given by Eqs. (6) and (7), respectively, we have

$$m_i \ddot{x}_i + m_i \omega_i^2 (1 + \alpha_i) x_i + \gamma x_e = 0, \tag{10}$$

$$m_e \ddot{x}_e + m_e \omega_e^2 [1 + \eta \cos(\omega_d t) + \alpha_e] x_e + \gamma x_i = 0, \tag{11}$$

where we have introduced the two shorthands

$$\alpha_{i(e)} = \frac{q_{i(e)}^2}{C_w m_{i(e)} \omega_{i(e)}^2 D_{i(e)}^2}, \tag{12}$$

$$\gamma = \frac{q_i q_e}{C_w D_i D_e}. \tag{13}$$

Therefore, the three parts of the total Hamiltonian introduced in Eq. (1) are explicitly given by

$$H_i = \frac{p_i^2}{2m_i} + \frac{1}{2} m_i \omega_i^2 (1 + \alpha_i) x_i^2, \tag{14}$$

$$H_e = \frac{p_e^2}{2m_e} + \frac{1}{2} m_e \omega_e^2 x_e^2 [1 + \alpha_e + \eta \cos(\omega_d t)], \tag{15}$$

$$H_I = \gamma x_i x_e, \tag{16}$$

where $p_{i(e)}$ represents the momentum of the ion (electron).

The equivalent circuit of this system is represented in Fig. 1(b), where the electric current $I_{i(e)}$ corresponds to the ion (electron) velocity [91], $L_{i(e)} = m_{i(e)} D_{i(e)}^2 / q_{i(e)}^2$ and $C_{i(e)} = [\omega_{i(e)}^2 L_{i(e)}]^{-1}$ denote the equivalent inductance and capacitance of the ion (electron) [73,78], respectively, and one has $1/C_e' = 1/C_e + 1/C_d$, with the capacitance $C_d = [\eta \cos(\omega_d t) \omega_e^2 L_e]^{-1}$ accounting for the driving field. Using the equivalent circuit elements, one obtains $\alpha_{i(e)} = C_{i(e)}/C_w$ and $\gamma = \pm\sqrt{m_i m_e / L_i L_e C_w^2}$. Here, we briefly note that $\omega_e/\omega_i \gg 1$ is expected under typical experimental conditions. Furthermore, this model can be extended straightforwardly to the case of multiple particles in each trap by considering the center-of-mass motion and making the replacements $q_{i(e)} \to N_{i(e)} q_{i(e)}$ and $m_{i(e)} \to N_{i(e)} m_{i(e)}$, where $N_{i(e)}$ is the number of ions (electrons) [75,76,78,91].

B. Effective coherent coupling

To illustrate the effective coherent coupling between the ions and electrons in such a setup, we rewrite the Hamiltonian (1) using annihilation and creation operators. Using the annihilation operator $a = \sqrt{m_i \omega_i'/2\hbar}(x_i + ip_i/m_i\omega_i')$ and suppressing the zero-point energy, the Hamiltonian of the ion motion can be directly rewritten as $H_i = \hbar\omega_i' a^\dagger a$, with the effective ion frequency $\omega_i' = \omega_i \sqrt{1 + \alpha_i}$.

The electron Hamiltonian, on the other hand, requires the transformation to an appropriate reference frame before it can be cast in the form $\tilde{H}_e = \hbar \partial_t \theta(t) b^\dagger b$, if we also omit the zero-point energy and define $\theta(t)$ as the phase of a special solution

$$f(t) = r(t) \exp[i\theta(t)] \tag{17}$$

of the Mathieu equation that constitutes the classical equation of motion under H_e [92–96]. The annihilation

operator of the electron motion thus reads

$$b = \sqrt{\frac{m_e W}{2\hbar}} \left(x_e + \frac{i}{m_e W} p_e \right) \tag{18}$$

and is time independent, since the Wronskian $W = (f^* \partial_t f - f \partial_t f^*)/2i = r^2 \partial_t \theta$ satisfies $\partial_t W = 0$ [96].

We note that the position of the electron, x_e, is rescaled to $r x_e$ in this reference frame, leading to the coupling

$$\tilde{H}_I = r\gamma x_i x_e = \frac{\hbar r \gamma}{2\sqrt{m_i m_e \omega_i' W}} (a + a^\dagger)(b + b^\dagger). \tag{19}$$

In the interaction picture with respect to H_i and $\tilde{H}_e$, where the annihilation operators transform according to $a \to a \exp(-i\omega_i' t)$ and $b \to b \exp[-i\theta(t)]$, we find the coupling Hamiltonian

$$\tilde{H}_I^{\mathrm{int}} = \frac{\hbar\gamma}{2\sqrt{m_i m_e \omega_i' W}} (a e^{-i\omega_i' t} + a^\dagger e^{i\omega_i' t})(b f^* + b^\dagger f). \tag{20}$$

The general form of $f(t)$ can be obtained by solving the classical motion of the electron under H_e, which is governed by

$$\ddot{x}_e + \omega_e'^2 \left[1 + \eta' \cos(\omega_d t)\right] x_e = 0, \tag{21}$$

where $\omega_e' = \omega_e \sqrt{1 + \alpha_e}$ is the effective electron frequency and $\eta' = \eta/(1 + \alpha_e)$ is the effective driving depth. This equation of motion can be transformed into the standard Mathieu equation [97]

$$\frac{d^2 x_e}{d\xi^2} + [A - 2Q\cos(2\xi)]x_e = 0, \tag{22}$$

using the substitutions

$$\xi = \frac{\omega_d t}{2}, \quad A = \frac{4\omega_e'^2}{\omega_d^2}, \quad Q = -\frac{A\eta'}{2}. \tag{23}$$

The Floquet solution of Eq. (22) is given by

$$f(\xi) = e^{i\mu\xi} \sum_{k=-\infty}^{\infty} c_k e^{i2k\xi}, \tag{24}$$

where μ is the characteristic exponent for the standard form of the Mathieu equation, and c_k is its kth Fourier coefficient [97–99] and we thereby find

$$f(t) = e^{i\mu\omega_d t/2} \sum_{k=-\infty}^{\infty} c_k e^{ik\omega_d t}. \tag{25}$$

Then, under the resonance condition

$$(\mu + 2k)\omega_d/2 = \omega_i', \tag{26}$$

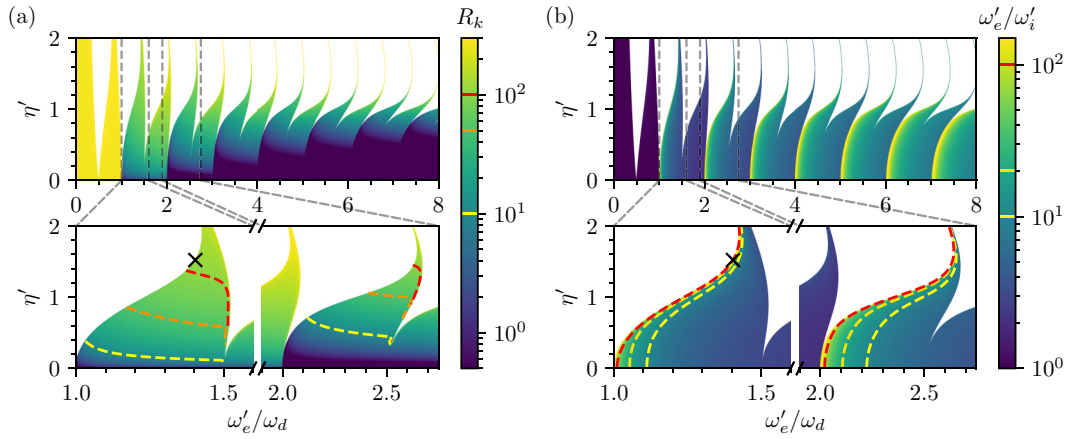the kth Fourier component of the electron motion will be resonant with the ion motion. We can therefore perform a

FIG. 2. (a) The relative coupling strength R_k for $k = 0$ across various values of η' and ω'_e/ω_d. (b) The ratio of ω'_e to ω'_i resulted from the resonant condition for $k = 0$ across various values of η' and ω'_e/ω_d. The areas with white color in both (a),(b) correspond to the regions with nonreal characteristic exponent μ, where the electron motion is unstable. The enlarged panels in both (a),(b) are depicted with contour lines in the regions bounded by $\mu = 0$ and $\mu = 1$. The values represented by the contour lines are indicated in the colorbars. The black cross denotes the typical parameters that we use in our further discussion.

rotating-wave approximation discarding highly oscillating terms in Eq. (20) and finally obtain

$$\tilde{H}_I^{\text{int}} \approx \hbar g_k(ab^\dagger + a^\dagger b), \tag{27}$$

where the coupling strength has the form

$$g_k = \frac{\gamma c_k}{2\sqrt{m_i m_e \omega'_i W}}, \tag{28}$$

with $c_k/\sqrt{W}$ decided by the driving-field parameters. The Hamiltonian (27) describes a coherent excitation exchange between ion and electron [2], enabling the sympathetic or exchange cooling of the electron motion [76,78].

III. DRIVING-FIELD PARAMETERS

We now analyze the relation between the driving-field parameters and the coupling strength under the resonance condition (26). To illustrate the enhancement of the coupling strength with respect to the ion-wire-ion coupling, we define the relative coupling strength

$$R_k = \left|\frac{g_k}{g_{ii}}\right| = D_k \sqrt{\frac{m_i}{m_e}}, \tag{29}$$

where $g_{ii} = 0.5\gamma/\omega'_i m_i$ is the ion-wire-ion coupling strength, and $D_k = |c_k|\sqrt{\omega_d(\mu + 2k)/2W}$ is a factor depending on the effective driving depth η' and the ratio of the effective electron frequency ω'_e to the driving frequency ω_d. Equation (29) shows that the enhancement is proportional to the square root of the mass ratio of ion to electron $\sqrt{m_i/m_e}$, which is, for example, around 269 for $^{40}\text{Ca}^+$ ions.

We then give a detailed derivation to show the dependence of D_k to the driving-field parameters. The characteristic exponent μ and the Fourier coefficients c_k in Eq. (24) can be numerically calculated for the specified parameters A and Q if we restrict $\text{Re}(\mu) \in [0, 2)$ and $\sum |c_k|^2 = 1$ [100]. With μ and c_k, the Wronskian with respect to ξ, $W_\xi = (f^*\partial_\xi f - f\partial_\xi f^*)/2i$, can be calculated by

$$\begin{aligned} W_\xi &= \frac{1}{2i}(f^*\partial_\xi f - f\,\partial_\xi f^*)|_{\xi=0} \\ &= \sum_{k,k'} c_k c'_{k'}(\mu + k + k'). \end{aligned} \tag{30}$$

Then we can obtain the Wronskian with respect to t by

$$W = \frac{\omega_d}{2}W_\xi. \tag{31}$$

The parameter D_k in Eq. (29) can then be expressed with W_ξ as

$$D_k = |c_k|\sqrt{\frac{\mu + 2k}{W_\xi}}. \tag{32}$$

Therefore, for any given ω'_e/ω_d and η', we can first calculate the corresponding A and Q and then obtain D_k using Eq. (32). Specifying $\sqrt{m_i/m_e}$ subsequently, the relative coupling strength R_k can be obtained.

Figure 2(a) illustrates the relative coupling strength R_k for different values of η' and ω'_e/ω_d with $k = 0$ and m_i equal to the mass of $^{40}\text{Ca}^+$. The colored (gray-scale) areas in Fig. 2(a), correspond to real values of the characteristic exponent μ and represent the electron-motion regions where stable solutions of the Mathieu equation
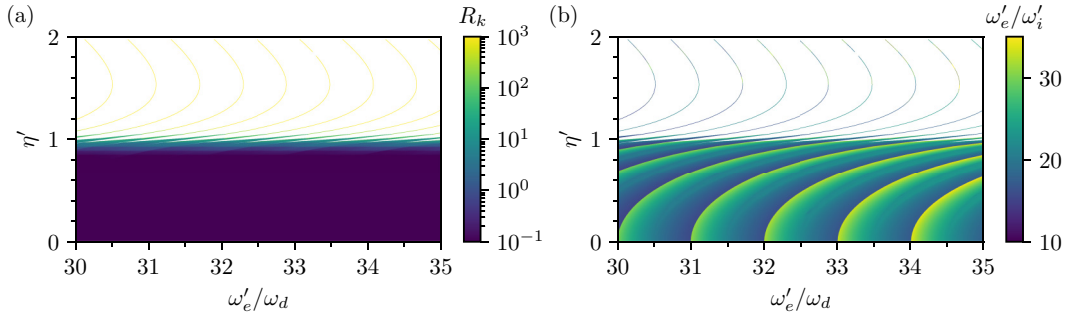
FIG. 3. (a) The relative coupling strength R_k with $k = 1$ across various values of η' and ω_e'/ω_d. (b) The ratio of ω_e' to ω_i' resulted from the resonant condition with $k = 1$ across various values of η' and ω_e'/ω_d.

exist, whereas the white areas correspond to nonreal μ and denote the regions of unstable electron motion. In addition, the boundaries of the stability regions correspond to integer μ [97]. As shown in Fig. 2(a), with increasing values of η', there is a concomitant increase in the relative coupling strength R_k, accompanied by a reduction in the size of the stable region. This puts a constraint on increasing η'. We further observe that, with increasing ω_e'/ω_d, the relative coupling strength R_k exhibits an overall decline across stable regions. This trend is illustrated by the expanded dark regions in Fig. 2(a) as ω_e'/ω_d increases. The enlarged panel of Fig. 2(a) compares two regions both delimited by a left boundary with $\mu = 0$ and a right boundary with $\mu = 1$. The contour lines in the enlarged panel of Fig. 2(a) overall shift upwards for the region with larger ω_e'/ω_d, indicating that a higher value of η' is required to achieve the same relative coupling strength R_k when parameters fall within the region with larger ω_e'/ω_d.

Using Eq. (26), the ratio ω_e'/ω_i' can be expressed as

$$\frac{\omega_e'}{\omega_i'} = \frac{\omega_e'}{\omega_d}\frac{2}{\mu + 2k}. \qquad (33)$$

Given that μ depends solely on η' and ω_e'/ω_d, Eq. (33) can be used to determine the ratio ω_e'/ω_i' for any given k, η' and ω_e'/ω_d. Figure 2(b) presents the numerically calculated ω_e'/ω_i' for $k = 0$ across various values of η' and ω_e'/ω_d. For regions corresponding to conventional experimental configurations with $\omega_e'/\omega_i' \gg 1$, it is found that $\mu \to 0$ and $\omega_e' > \omega_d$. Since ω_e'/ω_i' is proportional to ω_e'/ω_d, the light yellow areas in Fig. 2(b) expand as ω_e'/ω_d increases. The enlarged panel of Fig. 2(b) clearly shows that the contour lines overall shift to the center of the stable region for those with larger ω_e'/ω_d, indicating that a larger μ can be used to achieve the same ω_e'/ω_i' when parameters fall within the region with larger ω_e'/ω_d.

For $k \geq 1$ and conventional experimental configurations, where $\omega_e'/\omega_i' \gg 1$, Eq. (33) leads to

$$\frac{\omega_e'}{\omega_d} \gg k. \qquad (34)$$

Figure 3 takes $k = 1$ as an example, showing the relative coupling strength R_k under such condition. In this case, R_k gains significant magnitude largely in the very narrow stable region where $\eta' > 1$, which may result unstable trapping in experiments. Similar conclusion can also be found for the case of $k > 1$. Therefore, we mainly focus on the case of $k = 0$.

The black cross in Fig. 2 denotes a typical set of the potential parameters. This typical set is calculated in a reverse way. We first specify $\omega_d = 25\omega_i'$ and $k = 0$, which leads to $\mu = 2\omega_i'/\omega_d = 0.08$ according to the resonance condition of Eq. (26). We then set $Q = -6.0$ and calculate A reversely from μ and Q by constraining A into the specific stable region. In our case, we have $A \approx 7.88$. Then we can calculate $\eta' = -2Q/A \approx 1.52$ and $\omega_e' = \omega_d\sqrt{A}/2 \approx 35\omega_i'$. With this set of parameters, the relative coupling strength R_0 between single $^{40}Ca^+$ ions and single electrons is approximately 111.5 and the corresponding coupling strength may reach kilohertz regime for the Paul trap geometry demonstrated in Ref. [73].

IV. ELECTRON-MEDIATED ION-ION COUPLING

We now show that one can enhance the coupling between two separately trapped ions via an electron-mediated image-current interaction. The schematics of the model for Paul and Penning traps are shown in Figs. 4(a) and 4(b), respectively. In both setups, two separately trapped ion clouds are connected to the central electrons via two common electrodes. In Paul traps, the axial direction is perpendicular to the surfaces of the conductor wires [golden lines in Fig. 4(a)]. In Penning traps, the axial direction is horizontally along the ring electrodes [gray blocks in Fig. 4(b)]. This electron-mediated ion-ion coupling could be appealing for applications, such as qubit interconnection [73,101] and sympathetic cooling [74–76], and may also bring a revival of exchange cooling [78] due to the enhanced coupling rate.
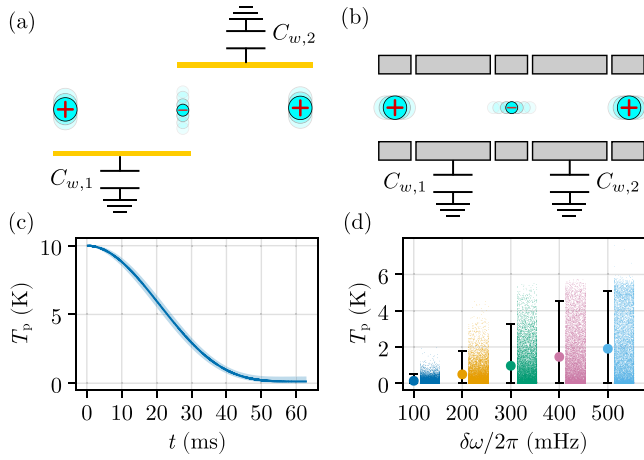
FIG. 4. (a) Schematic of electron-mediated ion-ion coupling for Paul traps. (b) Schematic of electron-mediated Be-proton coupling for Penning traps. The gray blocks represent cross-section views of the ring electrodes. $C_{w,1(2)}$ in (a),(b) is the capacitance of the common electrode 1(2) to ground. (c) Proton temperatures within one exchange ($t \in [0, t_{ex}]$) for $\delta\omega = (2\pi)100$ mHz. The solid line represents the proton average temperature and the band represents the 5%–95% range of the proton temperatures. (d) Proton temperatures at t_{ex} for $\delta\omega = (2\pi)[100, 200, \ldots, 500]$ mHz. Large scatters, error bars, and small scatters denote the proton average temperatures, the 5%–95% ranges of the proton temperatures and the proton temperature of every trajectory, respectively.

The Hamiltonian of the ion-electron-ion system in the interaction picture can be written as

$$\tilde{H}_{iei}^{int} = \sum_{j=1,2} \hbar g_j (e^{-i\delta_j t} a_j^\dagger b + \text{h.c.}), \qquad (35)$$

where g_j is the coupling strength between the center-of-mass motion of the electrons and the ions in the jth trap, as described by the annihilation operator a_j, and δ_j represents the corresponding frequency detuning.

As for quantum information processing, we envisage that such ion-ion coupling mediated by electrons can be utilized to construct deterministic entanglement of separately trapped single ions. First, we initialize two laser coolable and separately trapped single ions into the motional state $|1, 0\rangle$ at $t = 0$. Assuming that, in Eq. (35), $g_1 = g_2 = g$ and

$$\delta_1 = \delta_2 = \delta = \pm g\sqrt{\frac{8n^2}{2n+1}}, \quad n = 1, 3, 5, \ldots, \qquad (36)$$

the motional energies of the ions are fully exchanged, regardless of the initial state of the electrons, after the swap time

$$\tau_{swap} = \frac{\pi}{|g|}\sqrt{\frac{2n+1}{2}}. \qquad (37)$$

At $\tau_{swap}/2$, the motional quantum state of the two ions is in a maximally entangled state, namely in one of the two NOON states $(|1, 0\rangle \pm i|0, 1\rangle)/\sqrt{2}$ [102] (see Appendix A). The detuning δ is intentionally added to make the electron motion return to its initial state at $\tau_{swap}/2$, which is similar to the Mølmer-Sørensen gate for trapped ions [18,103,104]. For the ion-ion coupling with coupling strength g_{ii}, the swap time is $\pi/2g_{ii}$ [2]. Therefore, the gain of the ion-electron-ion coupling relative to the ion-ion coupling under similar experimental parameters can be expressed as

$$\text{gain} = \frac{\pi/2g_{ii}}{\tau_{swap}} = R_0\sqrt{\frac{1}{2(2n+1)}}, \qquad (38)$$

where R_0 is given by Eq. (29) with Fourier order $k = 0$. For two $^{40}\text{Ca}^+$ ions trapped separately, the coupling gain is approximately 45.5 with $n = 1$ and the driving parameters indicated by the black cross in Fig. 2.

For a near symmetric and resonant case, the two ion clouds in separated traps will almost fully exchange their energy at

$$t_{ex} = \frac{\pi}{\sqrt{g_1^2 + g_2^2}}, \qquad (39)$$

regardless of the initial state of the electrons, which can be utilized to achieve exchange cooling. To illustrate this, we numerically simulate the electron-mediated energy exchange process between $^9\text{Be}^+$ ions and a single proton in the classical regime. All simulation parameters are referenced from well-developed Penning trap experiments [75–77]. The effective electrode distances are set to $-D_{1,\text{Be}} = D_{1,e} = -D_{2,e} = D_{2,\text{P}} = 3.2$ mm, where the first subscript denotes the electrode number, the second subscript denotes the particle species, and $\pm$ is decided by the relative position of the particles to the electrodes. The capacitances of the electrodes are set to $C_{w,1} = C_{w,2} = 5.5$ pF. The effective trapping frequencies of Be and proton are $\omega'_{\text{Be}} = \omega'_{\text{P}} = (2\pi)354.25$ kHz, and the driving frequency, effective driving depth and effective trapping frequency of the electron trap, denoted by the black cross in Fig. 2, are $\omega_d = 25\omega'_{\text{Be}}$, $\eta' \approx 1.52$, and $\omega'_e \approx 35\omega'_{\text{Be}}$, respectively. The ratio of the number of Be ions N_{Be} to the number of protons N_{P} is chosen to be approximately equal to the ratio of m_{Be} to m_{P}, which insures that g_1 and g_2 in Eq. (35) are approximately equal in the symmetric trap configuration. For the single-proton case, we have $N_{\text{Be}} = 9$. The electron number N_e is set in the simulation to 1000, a value that is attainable in experimental settings [105–107]. The coupling constants $\gamma_{\text{Be},e}$ and $\gamma_{\text{P},e}$ can be obtained with Eq. (13). Using Eq. (28), we then obtain the corresponding coupling rates $g_1 \approx g_2 \approx (2\pi)5.6$ Hz. The coupling gain, relative to the Be-proton wire-mediated coupling with $N_{\text{Be}} = 1000$ and

$N_P = 1$, can also be calculated using Eq. (38) with $n = 0$ and considering the mass and particle number modifications to R_0. In this case, the coupling gain is approximately 37.5.

Our simulation takes into account the relative frequency uncertainties by randomly adding normal-distributed detunings with standard deviation $\delta\omega$ to the electron and proton trap for every simulation trajectory, see Appendix B. Other heating noise is negligibly small for a cryogenic Penning trap. The simulation results are obtained from 10 000 trajectories for each $\delta\omega$ with the Be cloud initially cooled to 0.5 mK, near the Doppler limit [76], and the temperatures of the electron cloud and the single proton are both equal to 10 K. The relative initial phases of the proton and the electrons motion are randomly chosen from $[0, 2\pi]$, see Appendix B. The proton average temperature for $\delta\omega = (2\pi)100$ mHz is depicted by the solid line in Fig. 4(c). After a single exchange, at $t_{ex} \approx 63$ ms, the proton average temperature reaches 133.4 mK. Figure 4(d) shows the dependence of the cooling performance on the frequency uncertainty. Even for $\delta\omega = (2\pi)500$ mHz, the temperature of the proton decreases 81% on average within a single exchange (63 ms), reaching 1.9 K.

V. CONCLUSION

In this work, we presented a wire-mediated scheme for coherent ion-electron coupling with a two-orders-of-magnitude-enhanced strength, compared to known wire-mediated ion-ion coupling. For mere single ions and electrons, our analysis shows that the ion-electron coupling strength may reach kilohertz regime in feasible experimental setups. With demonstrated techniques for ion-trap noise reduction, such as Ar^+ bombardment [108] and operation at cryogenic temperatures [109], the electron-mediated image-current coupling between ions would be competitive with existing remote-coupling methods based on ion shuttling [38,110] or photon linking [111,112], regarding quantum information processing. Further numerical simulations of electron-mediated exchange cooling of single protons in low-noise Penning traps [113,114] highlight the potential application of our scheme for precision measurements. Our work thereby lays the groundwork for the development of various hybrid platforms with promising prospects for electron-mediated coupling of ions to a broad range of systems, from microscopic particles like antiprotons to macroscopic devices like *LC* circuits [25].

APPENDIX A: DETAILS ON ELECTRON-MEDIATED ION-ION COUPLING

Here, we give a detailed analysis on ion-electron-ion motion coupling for deterministic entanglement generation and exchange cooling in a rotating frame where the Hamiltonian is time independent.

As for deterministic entanglement generation, assuming $g = g_1 = g_2$ and $\delta = \delta_1 = \delta_2$, we have

$$\tilde{H}_{iei}^{int'} = \hbar\delta b^\dagger b + g[(a_1^\dagger + a_2^\dagger)b + \text{H.c.}]. \quad (A1)$$

Generally, the initial state can be written as

$$|\psi(t)\rangle = \sum_{n_1,n_2,n_3} c_{n_1,n_2,n_3}(t)|n_1, n_2, n_3\rangle, \quad (A2)$$

where $c_{n_1,n_2,n_3}(t)$ is the probability amplitude of the state $|n_1, n_2, n_3\rangle$ with n_1, n_2, and n_3, representing the phonon numbers for ion 1, ion 2 and electron, respectively. Using

$$i\hbar\frac{\partial|\psi\rangle}{\partial t} = \tilde{H}_{iei}^{int'}|\psi\rangle, \quad (A3)$$

we have

$$\begin{aligned}
i\dot{c}_{n_1,n_2,n_3} = {}& \delta n_3 c_{n_1,n_2,n_3} \\
&+ g\sqrt{n_3+1}\sqrt{n_1}\,c_{n_1-1,n_2,n_3+1} \\
&+ g\sqrt{n_3+1}\sqrt{n_2}\,c_{n_1,n_2-1,n_3+1} \\
&+ g\sqrt{n_3}\sqrt{n_1+1}\,c_{n_1+1,n_2,n_3-1} \\
&+ g\sqrt{n_3}\sqrt{n_2+1}\,c_{n_1,n_2+1,n_3-1}, \quad (A4)
\end{aligned}$$

where $[\dot{\ }]$ stands for $\partial/\partial t$. For a total phonon number equal to 1, we can simplify Eq. (A4) to

$$i\dot{c}_{100} = g c_{001}, \quad (A5)$$

$$i\dot{c}_{010} = g c_{001}, \quad (A6)$$

$$i\dot{c}_{001} = \delta c_{001} + g c_{100} + g c_{010}. \quad (A7)$$

With initial conditions $c_{100} = 1$, $c_{010} = 0$, and $c_{001} = 0$, the solution for the probability amplitudes is

$$\begin{aligned}
c_{100}(t) = {}& \frac{1}{2} + \frac{e^{-\frac{1}{2}igt\delta_r}}{2}\cos\left(\frac{1}{2}gt\sqrt{8+\delta_r^2}\right) \\
&+ \frac{i\delta_r e^{-\frac{1}{2}igt\delta_r}}{2\sqrt{8+\delta_r^2}}\sin\left(\frac{1}{2}gt\sqrt{8+\delta_r^2}\right), \quad (A8)
\end{aligned}$$

$$c_{010}(t) = -\frac{1}{2} + \frac{e^{-\frac{1}{2}igt\delta_r}}{2}\cos\left(\frac{1}{2}gt\sqrt{8+\delta_r^2}\right)$$
$$+ \frac{i\delta_r e^{-\frac{1}{2}igt\delta_r}}{2\sqrt{8+\delta_r^2}}\sin\left(\frac{1}{2}gt\sqrt{8+\delta_r^2}\right), \quad \text{(A9)}$$

$$c_{001}(t) = -\frac{2ie^{-\frac{1}{2}igt\delta_r}}{\sqrt{8+\delta_r^2}}\sin\left(\frac{1}{2}gt\sqrt{8+\delta_r^2}\right), \quad \text{(A10)}$$

where we defined $\delta_r = \delta/g$. At the end of the evolution, $t = \tau$, we expect $c_{001}(\tau) = 0$, which is fulfilled if

$$\frac{1}{2}g\tau\sqrt{8+\delta_r^2} = m\pi, \quad \text{(A11)}$$

with an integer m. Substituting Eq. (A11) into Eqs. (A8) and (A9), we thereby find

$$c_{100}(\tau) = \frac{1}{2}\left[1 + (-1)^m e^{-\frac{1}{2}ig\tau\delta_r}\right], \quad \text{(A12)}$$

$$c_{010}(\tau) = \frac{1}{2}\left[-1 + (-1)^m e^{-\frac{1}{2}ig\tau\delta_r}\right] \quad \text{(A13)}$$

and if one now requires

$$-\frac{1}{2}g\tau\delta_r = n\frac{\pi}{2}, \quad \text{(A14)}$$

with another integer n and combines this condition with Eq. (A11), one arrives at

$$\delta = \pm g\sqrt{\frac{8n^2}{(2m)^2 - n^2}}, \quad \text{(A15)}$$

$$\tau = \frac{\pi}{2|g|}\sqrt{\frac{(2m)^2 - n^2}{2}}, \quad \text{(A16)}$$

where $m, n \in \mathbb{Z}$ and $|2m| > |n|$.

If n is odd, we substitute Eq. (A14) into Eqs. (A12) and (A13), obtaining

$$c_{100}(\tau) = \frac{1}{2}\left\{1 + i(-1)^{\left[m+\frac{n-1}{2}\right]}\right\}, \quad \text{(A17)}$$

$$c_{010}(\tau) = \frac{1}{2}\left\{-1 + i(-1)^{\left[m+\frac{n-1}{2}\right]}\right\}, \quad \text{(A18)}$$

which means the motion of the two ions is in one of the NOON states $(|1,0\rangle \pm i|0,1\rangle)/\sqrt{2}$ at $t = \tau$. Without loss of generality, we can assume $n, m > 0$. If we substitute $2m$

with $n + 1$, we can obtain

$$\delta = \pm g\sqrt{\frac{8n^2}{2n+1}}, \quad \text{(A19)}$$

$$\tau = \frac{\pi}{2|g|}\sqrt{\frac{2n+1}{2}}, \quad \text{(A20)}$$

where we find that $\tau = \tau_{\text{swap}}/2$ with τ_{swap} defined by the Eq. (37). On the other hand, if n is even, we substitute Eqs. (A14) into Eqs. (A12) and (A13), obtaining

$$c_{100}(\tau) = \frac{1}{2}\left\{1 + (-1)^{m+\frac{n}{2}}\right\}, \quad \text{(A21)}$$

$$c_{010}(\tau) = \frac{1}{2}\left\{-1 + (-1)^{m+\frac{n}{2}}\right\}, \quad \text{(A22)}$$

which means that, at $t = \tau$, the two ions are either in their initial states for even $m + n/2$ or fully exchange their energies for odd $m + n/2$. For the full-exchange case with even m (namely $m + n/2$ is odd and m is even), by rewriting Eq. (A16) as

$$\tau = \frac{\pi}{|g|}\sqrt{\frac{m^2 - \left(\frac{n}{2}\right)^2}{2}}, \quad \text{(A23)}$$

we find that $\tau/2$ in such a case is equivalent to τ with odd n. This means that the two ions not only exchange their energies at $t = \tau$ in such a case, but are also in a NOON state at $t = \tau/2$. However, for the full-exchange case with odd m, $\tau/2$ is not equivalent to τ with odd n and the noninteger $m/2$ results $c_{001}(\tau/2) \neq 0$, which means that the two ions are not in a NOON state at $\tau/2$.

In summary, we can substitute $n/2$ in Eq. (A23) with integer n and obtain

$$\tau = \tau_{\text{swap}} = \frac{\pi}{|g|}\sqrt{\frac{m^2 - n^2}{2}}, \quad \text{(A24)}$$

where $m, n \in \mathbb{Z}$, $|m| > |n|$ and $m + n$ is odd. Only when n is odd, the two ions are in a NOON states at $t = \tau_{\text{swap}}/2$. Setting $m = n + 1$, we have

$$\tau_{\text{swap}} = \frac{\pi}{|g|}\sqrt{\frac{2n+1}{2}}, \quad \text{(A25)}$$

which is Eq. (37).

Although we assume the initial phonon number of the electron is zero, the results we obtained here are actually not dependent on the initial phonon number of the electron.

We then discuss this argument in Heisenberg's picture. In Heisenberg's picture, we have

$$a_1(t) = \frac{1}{2}\left[a_1(0) - a_2(0) + h(t)\right], \tag{A26}$$

$$a_2(t) = \frac{1}{2}\left[a_2(0) - a_1(0) + h(t)\right], \tag{A27}$$

$$b(t) = -\frac{i\left[2a_1(0) + 2a_2(0) + \delta_r b(0)\right]}{e^{igt\delta_r/2}\sqrt{8 + \delta_r^2}}\sin\left(\frac{gt\sqrt{8 + \delta_r^2}}{2}\right)$$
$$+ e^{-igt\delta_r/2}b(0)\cos\left(\frac{gt\sqrt{8 + \delta_r^2}}{2}\right), \tag{A28}$$

where

$$h(t) = e^{-igt\delta_r/2}\left[a_1(0) + a_2(0)\right]\cos\left(\frac{gt\sqrt{8 + \delta_r^2}}{2}\right)$$
$$+ \frac{i\left[\delta_r\left(a_1(0) + a_2(0)\right) - 4b(0)\right]}{e^{igt\delta_r/2}\sqrt{8 + \delta_r^2}}\sin\left(\frac{gt\sqrt{8 + \delta_r^2}}{2}\right). \tag{A29}$$

At $t = \tau$, substituting $g\tau\sqrt{8 + \delta_r^2}/2$ with Eq. (A11), we have

$$a_1(\tau) = \frac{1}{2}a_1(0)\left[1 + (-1)^m e^{-ig\tau\delta_r/2}\right]$$
$$+ \frac{1}{2}a_2(0)\left[-1 + (-1)^m e^{-ig\tau\delta_r/2}\right], \tag{A30}$$

$$a_2(\tau) = \frac{1}{2}a_2(0)\left[1 + (-1)^m e^{-ig\tau\delta_r/2}\right]$$
$$+ \frac{1}{2}a_1(0)\left[-1 + (-1)^m e^{-ig\tau\delta_r/2}\right], \tag{A31}$$

$$b(\tau) = (-1)^m b(0)e^{-ig\tau\delta_r/2}. \tag{A32}$$

We see that $a_1(\tau)$ and $a_2(\tau)$ is not dependent on $b(0)$, which means that the results we mentioned before are not dependent on the initial motional state of the electron.

We then discuss the resonant case for exchange cooling. For $g_1 \neq g_2$ but $\delta_1 = \delta_2 = 0$, defining $g = \sqrt{g_1^2 + g_2^2}$, in Heisenberg's picture, we have

$$a_1(t) = a_1(0)\left[\frac{g_1^2}{g^2}\cos(gt) + \frac{g_2^2}{g^2}\right] - ib(0)\frac{g_1}{g}\sin(gt)$$
$$+ a_2(0)\frac{g_1 g_2}{g^2}[\cos(gt) - 1], \tag{A33}$$

$$a_2(t) = a_2(0)\left[\frac{g_2^2}{g^2}\cos(gt) + \frac{g_1^2}{g^2}\right] - ib(0)\frac{g_2}{g}\sin(gt)$$
$$+ a_1(0)\frac{g_1 g_2}{g^2}[\cos(gt) - 1], \tag{A34}$$

$$b(t) = b(0)\cos(gt) - i\frac{a_1(0)g_1 + a_2(0)g_2}{g}\sin(gt). \tag{A35}$$

These equations can be utilized to obtain the energy exchange of the classical motion by assuming the initial state to be a direct product state of coherent states, $|\alpha_1, \alpha_2, \beta\rangle$. The center-of-mass energies of the separately trapped particles can be written as

$$E_1(t) = \hbar\omega\left\langle a_1^\dagger(t)a_1(t)\right\rangle = \hbar\omega\left|\alpha_1(t)\right|^2, \tag{A36a}$$

$$E_2(t) = \hbar\omega\left\langle a_2^\dagger(t)a_2(t)\right\rangle = \hbar\omega\left|\alpha_2(t)\right|^2, \tag{A36b}$$

$$E_b(t) = \hbar\omega_b\left\langle b^\dagger(t)b(t)\right\rangle = \hbar\omega_b\left|\beta(t)\right|^2, \tag{A36c}$$

where

$$\alpha_1(t) = \alpha_2\frac{g_1 g_2}{g^2}[\cos(gt) - 1] + \alpha_1\frac{g_1^2}{g^2}\left[\cos(gt) + \frac{g_2^2}{g_1^2}\right]$$
$$- i\beta\frac{g_1}{g}\sin(gt), \tag{A37}$$

$$\alpha_2(t) = \alpha_1\frac{g_1 g_2}{g^2}[\cos(gt) - 1] + \alpha_2\frac{g_2^2}{g^2}\left[\cos(gt) + \frac{g_1^2}{g_2^2}\right]$$
$$- i\beta\frac{g_2}{g}\sin(gt), \tag{A38}$$

$$\beta(t) = \beta\cos(gt) - i\frac{\alpha_1 g_1 + \alpha_2 g_2}{g}\sin(gt), \tag{A39}$$

ω is the frequency of the two separately trapped ions, and ω_b is the effective frequency of the electron under the driving field, which can be determined by the ratio of the electron average motional energy to the corresponding Fock number. From Eqs. (A36), we can find that, if $g_1 = g_2$, at time $t_{ex} = \pi/g$, the energies of ions are fully exchanged.
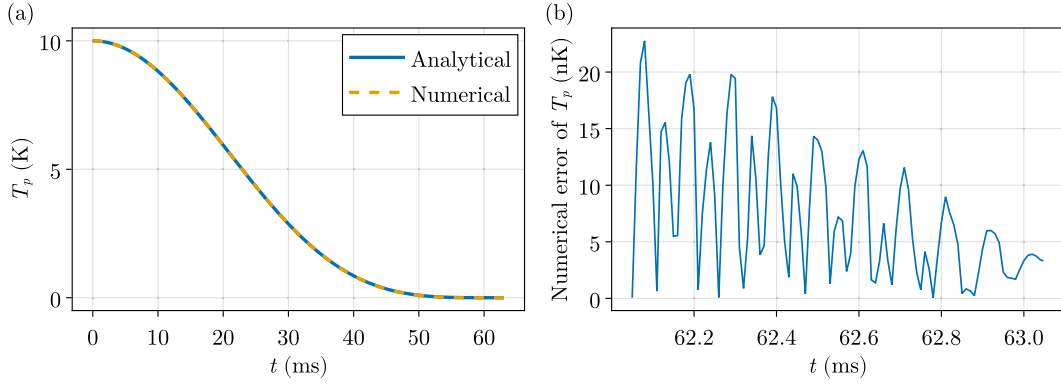
FIG. 5. (a) Analytical (solid blue line) and numerical (dashed yellow line) solutions of the proton temperature T_p within a single exchange. (b) Numerical error of the proton temperature around the end of the exchange.

APPENDIX B: NUMERICAL DETAILS ON EXCHANGE COOLING

In the simulation of exchange cooling, we consider 9 $^9\text{Be}^+$ ions, 1000 electrons and a single proton. The couplings between traps are mediated via common electrodes. The classical motion of the system is governed by

$$\ddot{x}_{\text{Be}} + \omega_{\text{Be}}'^2 x_{\text{Be}} + \frac{\gamma_{\text{Be},e}}{N_{\text{Be}} m_{\text{Be}}} x_e$$

$$= \ddot{x}_e + \omega_e'^2 [1 + \eta' \cos(\omega_d t)] x_e + \frac{\gamma_{\text{Be},e}}{N_e m_e} x_{\text{Be}} + \frac{\gamma_{\text{P},e}}{N_e m_e} x_{\text{P}}$$

$$= \ddot{x}_{\text{P}} + \omega_{\text{P}}'^2 x_{\text{P}} + \frac{\gamma_{\text{P},e}}{N_{\text{P}} m_{\text{P}}} x_e = 0, \qquad (B1)$$

where x_{Be}, x_e, x_{P} are the center-of-mass positions of the $^9\text{Be}^+$ ions, the electrons and the single proton, respectively. The numerical integration of Eq. (B1) uses the 12th-order explicit adaptive Runge-Kutta-Nyström method provided by `DifferentialEquations.jl` [115] with step-size control options abstol $= 1.0 \times 10^{-12}$, reltol $= 1.0 \times 10^{-12}$, and number type `Double64` provided by `DoubleFloats.jl` [116]. The number type `Double64` has a significand of 106 bits, two times larger than that of the common number type `Float64`.

To make sure that the finite numerical precision does not negatively affect our simulation results, we compare our simulation results with the theoretical analysis. Substituting the subscript 1 and 2 of E and α in Eq. (A36) with Be and P and setting $\beta = 0$ and α_{Be} and α_{P} in the same phase, we have

$$E_{\text{Be}}(t) = \left| \sqrt{E_{\text{P}}(0)} \frac{g_1 g_2}{g^2} [\cos(gt) - 1] \right.$$

$$\left. + \sqrt{E_{\text{Be}}(0)} \frac{g_1^2}{g^2} \left[\cos(gt) + \frac{g_2^2}{g_1^2} \right] \right|^2, \qquad (B2)$$

$$E_{\text{P}}(t) = \left| \sqrt{E_{\text{Be}}(0)} \frac{g_1 g_2}{g^2} [\cos(gt) - 1] \right.$$

$$\left. + \sqrt{E_{\text{P}}(0)} \frac{g_2^2}{g^2} \left[\cos(gt) + \frac{g_1^2}{g_2^2} \right] \right|^2, \qquad (B3)$$

which corresponds to the initial condition: $x_e(0) = x_{\text{Be}}(0) = x_{\text{P}}(0) = 0$ μm, $\dot{x}_e(0) = 0$, $\dot{x}_{\text{Be}}(0) = \sqrt{2E_{\text{Be}}(0)/m_{\text{Be}}}$, and $\dot{x}_{\text{P}}(0) = \sqrt{2E_{\text{P}}(0)/m_{\text{P}}}$. Defining $T_{\text{Be}} = E_{\text{Be}}/k_B$ and $T_{\text{P}} = E_{\text{P}}/k_B$, we can obtain the solid blue line in Fig. 5(a) using Eq. (B3) with $T_{\text{Be}}(0) = 0.5$ mK and $T_{\text{P}}(0) = 10$ K. The dashed yellow line in Fig. 5(a) shows the numerical result of $T_{\text{P}}(t)$ within a single exchange, which is nearly identical to the theoretical one. Around the end of the exchange, the energy deviation of the simulation result from the theoretical one is only a few nK $\times k_B$, as shown in Fig. 5(b). This numerical accuracy is sufficient for our case. Figure 6 shows the center-of-mass position trajectory of the electrons around $t_{\text{ex}}/2$, where the electrons reach the max amplitude during the exchange process.

Figures 4(c) and 4(d) are obtained from 10 000 trajectories for each standard deviation $\delta\omega$. Besides the random
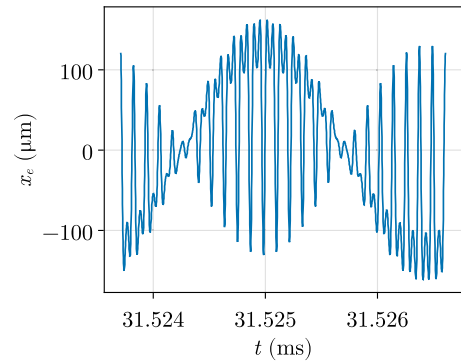

FIG. 6. Electron dynamics around the midpoint of the exchange process.

detunings, every trajectory also takes into account the random phases of the initial modes. Other sources of noise are negligible in the cryogenic Penning trap [76,114]. Equations (A36) indicate that only relative initial phases will influence the energy of motion during exchange. Therefore, we randomly add relative initial phases ϕ_P and ϕ_e to the proton and electron initial state, respectively, and set the Be ion initial phase to 0. For the single proton with initial temperature T_P and relative phase ϕ_P, we have

$$x_P(0) = \frac{2k_B T_P}{m_P \omega_P'^2} \sin(\phi_P), \tag{B4}$$

$$\dot{x}_P(0) = \frac{2k_B T_P}{m_P} \cos(\phi_P). \tag{B5}$$

As for electrons, it is appropriate to define the electron temperature by the kinetic energy averaged over the infinite time t':

$$E_{\mathrm{kin},e} = \lim_{t' \to \infty} \frac{1}{t'} \int_0^{t'} \frac{1}{2} m_e \dot{x}_e^2 \, dt = \frac{1}{2} k_B T_e. \tag{B6}$$

To see the relationship between T_e and the electron motion amplitude, we rewrite Eq. (25) into a form with sine functions:

$$x_e(t) = A_e f_s(t) = A_e \sum_{k=-\infty}^{\infty} c_k \sin\left[(\mu + 2k)\frac{\omega_d t}{2}\right], \tag{B7}$$

where A_e is the amplitude of the electron motion. Immediately, we can write down the electron velocity as

$$\dot{x}_e(t) = \frac{A_e \omega_d}{2} \sum_{k=-\infty}^{\infty} (\mu + 2k) c_k \cos\left[(\mu + 2k)\frac{\omega_d t}{2}\right]. \tag{B8}$$

With Parseval's theorem [117], we obtain

$$\lim_{t' \to \infty} \frac{1}{t'} \int_0^{t'} \frac{1}{2} m_e \dot{x}_e^2 \, dt = \frac{A_e^2 \omega_d^2}{8} \sum_{k=-\infty}^{\infty} |(\mu + 2k)c_k|^2. \tag{B9}$$

Substituting Eq. (B9) into Eq. (B6) and using the definition $S = \sum_{k=-\infty}^{\infty} |(\mu + 2k)c_k|^2$, we obtain

$$A_e = \sqrt{\frac{8k_B T_e}{m_e \omega_d^2 S}}. \tag{B10}$$

With the relative phase ϕ_e, we have

$$x_e(0) = A_e \sin(\phi_e) \sum_{k=-\infty}^{\infty} c_k, \tag{B11}$$

$$\dot{x}_e(0) = \frac{A_e \omega_d}{2} \cos(\phi_e) \sum_{k=-\infty}^{\infty} (\mu + 2k)c_k. \tag{B12}$$

To sum up, for every simulation trajectory, we first randomly generate ϕ_P and ϕ_e in the $[0, 2\pi]$ range to obtain the initial motional state using Eqs. (B4) and (B5) and Eqs. (B11) and (B12). Then, we modify ω_e' and ω_P' with two randomly generated relative detunings, whose standard deviations are both set to $\delta\omega$. Next, we integrate Eqs. (B1) with numerical configurations mentioned above to obtain the original data for Figs. 4(b) and 4(c).

With Eq. (B10), we can also calculate the effective frequency ω_b mentioned in Eq. (A36c). Equation (B10) can be rewritten as

$$k_B T_e = \frac{A_e^2 m_e \omega_d^2 S}{8}. \tag{B13}$$

For a coherent state $|\beta\rangle$, we have

$$k_B T_e = \hbar \omega_b |\beta|^2. \tag{B14}$$

Therefore, we obtain

$$\hbar \omega_b |\beta|^2 = \frac{A_e^2 m_e \omega_d^2 S}{8}. \tag{B15}$$

According to the transformations made to obtain $\tilde{H}_e$, the classical amplitude A_e is connected to the coherent state $|\beta\rangle$ by

$$A_e = |\beta| \sqrt{\frac{2\hbar}{m_e W}}, \tag{B16}$$

where W is the Wronskian defined in Eq. (31). Substituting Eq. (B16) into Eq. (B15) and utilizing Eq. (31), we obtain

$$\omega_b = \frac{\omega_d S}{2 W_\xi}. \tag{B17}$$

For the driving-field parameters that we choose in our simulation, ω_b is approximately $(2\pi)142$ MHz.

[1] T. Gaebel, M. Domhan, I. Popa, C. Wittmann, P. Neumann, F. Jelezko, J. R. Rabeau, N. Stavrias, A. D. Greentree, S. Prawer, J. Meijer, J. Twamley, P. R. Hemmer, and J. Wrachtrup, Room-temperature coherent coupling of single spins in diamond, Nat. Phys. **2**, 408 (2006).

[2] K. R. Brown, C. Ospelkaus, Y. Colombe, A. C. Wilson, D. Leibfried, and D. J. Wineland, Coupled quantized mechanical oscillators, Nature (London) **471**, 196 (2011).

[3] M. Harlander, R. Lechner, M. Brownnutt, R. Blatt, and W. Hänsel, Trapped-ion antennae for the transmission of quantum information, Nature (London) **471**, 200 (2011).

[4] J. Cai, A. Retzker, F. Jelezko, and M. B. Plenio, A large-scale quantum simulator on a diamond surface at room temperature, Nat. Phys. **9**, 168 (2013).

[5] A. C. Wilson, Y. Colombe, K. R. Brown, E. Knill, D. Leibfried, and D. J. Wineland, Tunable spin–spin interactions and entanglement of ions in separate potential wells, Nature (London) **512,** 57 (2014).

[6] J. J. Viennot, M. C. Dartiailh, A. Cottet, and T. Kontos, Coherent coupling of a single spin to microwave cavity photons, Science **349,** 408 (2015).

[7] J. I. Cirac and P. Zoller, Quantum computations with cold trapped ions, Phys. Rev. Lett. **74,** 4091 (1995).

[8] C. Monroe, D. M. Meekhof, B. E. King, W. M. Itano, and D. J. Wineland, Demonstration of a fundamental quantum logic gate, Phys. Rev. Lett. **75,** 4714 (1995).

[9] J. F. Poyatos, J. I. Cirac, and P. Zoller, Quantum gates with "hot" trapped ions, Phys. Rev. Lett. **81,** 1322 (1998).

[10] K. Mølmer and A. Sørensen, Multiparticle entanglement of hot trapped ions, Phys. Rev. Lett. **82,** 1835 (1999).

[11] A. Sørensen and K. Mølmer, Quantum computation with ions in thermal motion, Phys. Rev. Lett. **82,** 1971 (1999).

[12] C. A. Sackett, D. Kielpinski, B. E. King, C. Langer, V. Meyer, C. J. Myatt, M. Rowe, Q. A. Turchette, W. M. Itano, D. J. Wineland, and C. Monroe, Experimental entanglement of four particles, Nature (London) **404,** 256 (2000).

[13] F. Schmidt-Kaler, H. Häffner, M. Riebe, S. Gulde, G. P. T. Lancaster, T. Deuschle, C. Becher, C. F. Roos, J. Eschner, and R. Blatt, Realization of the Cirac–Zoller controlled-NOT quantum gate, Nature (London) **422,** 408 (2003).

[14] C. F. Roos, M. Riebe, H. Häffner, W. Hänsel, J. Benhelm, G. P. T. Lancaster, C. Becher, F. Schmidt-Kaler, and R. Blatt, Control and measurement of three-qubit entangled states, Science **304,** 1478 (2004).

[15] P. O. Schmidt, T. Rosenband, C. Langer, W. M. Itano, J. C. Bergquist, and D. J. Wineland, Spectroscopy using quantum logic, Science **309,** 749 (2005).

[16] X. Zhu, S. Saito, A. Kemp, K. Kakuyanagi, S.-I. Karimoto, H. Nakano, W. J. Munro, Y. Tokura, M. S. Everitt, K. Nemoto, M. Kasu, N. Mizuochi, and K. Semba, Coherent coupling of a superconducting flux qubit to an electron spin ensemble in diamond, Nature (London) **478,** 221 (2011).

[17] A. Stute, B. Casabone, P. Schindler, T. Monz, P. O. Schmidt, B. Brandstätter, T. E. Northup, and R. Blatt, Tunable ion–photon entanglement in an optical cavity, Nature (London) **485,** 482 (2012).

[18] N. Daniilidis, D. J. Gorman, L. Tian, and H. Häffner, Quantum information processing with trapped electrons and superconducting electronics, New J. Phys. **15,** 073017 (2013).

[19] N. Daniilidis and H. Häffner, Quantum interfaces between atomic and solid-state systems, Annu. Rev. Condens. Matter Phys. **4,** 83 (2013).

[20] J. Cai, F. Jelezko, and M. B. Plenio, Hybrid sensors based on colour centres in diamond and piezoactive layers, Nat. Commun. **5,** 4065 (2014).

[21] Y. Tabuchi, S. Ishino, A. Noguchi, T. Ishikawa, R. Yamazaki, K. Usami, and Y. Nakamura, Coherent coupling between a ferromagnetic magnon and a superconducting qubit, Science **349,** 405 (2015).

[22] C. J. Ballance, V. M. Schäfer, J. P. Home, D. J. Szwer, S. C. Webster, D. T. C. Allcock, N. M. Linke, T. P. Harty, D.

P. L. Aude Craik, D. N. Stacey, A. M. Steane, and D. M. Lucas, Hybrid quantum logic and a test of Bell's inequality using two different atomic isotopes, Nature (London) **528,** 384 (2015).

[23] T. R. Tan, J. P. Gaebler, Y. Lin, Y. Wan, R. Bowler, D. Leibfried, and D. J. Wineland, Multi-element logic gates for trapped-ion qubits, Nature (London) **528,** 380 (2015).

[24] Y. Wang, M. Um, J. Zhang, S. An, M. Lyu, J.-N. Zhang, L.-M. Duan, D. Yum, and K. Kim, Single-qubit quantum memory exceeding ten-minute coherence time, Nat. Photonics **11,** 646 (2017).

[25] S. Kotler, R. W. Simmonds, D. Leibfried, and D. J. Wineland, Hybrid quantum systems with trapped charged particles, Phys. Rev. A **95,** 022327 (2017).

[26] C. J. Foot, D. Trypogeorgos, E. Bentine, A. Gardner, and M. Keller, Two-frequency operation of a Paul trap to optimise confinement of two species of ions, Int. J. Mass Spectrom. **430,** 117 (2018).

[27] T. M. Karg, B. Gouraud, C. T. Ngai, G.-L. Schmid, K. Hammerer, and P. Treutlein, Light-mediated strong coupling between a mechanical oscillator and atomic spins 1 meter apart, Science **369,** 174 (2020).

[28] P. Weckesser, F. Thielemann, D. Wiater, A. Wojciechowska, L. Karpa, K. Jachymski, M. Tomza, T. Walker, and T. Schaetz, Observation of Feshbach resonances between a single ion and ultracold atoms, Nature (London) **600,** 429 (2021).

[29] J. I. Cirac and P. Zoller, A scalable quantum computer with ions in an array of microtraps, Nature (London) **404,** 579 (2000).

[30] S. Gulde, M. Riebe, G. P. T. Lancaster, C. Becher, J. Eschner, H. Häffner, F. Schmidt-Kaler, I. L. Chuang, and R. Blatt, Implementation of the Deutsch–Jozsa algorithm on an ion-trap quantum computer, Nature (London) **421,** 48 (2003).

[31] H. Häffner, W. Hänsel, C. F. Roos, J. Benhelm, D. Chekal-kar, M. Chwalla, T. Körber, U. D. Rapol, M. Riebe, P. O. Schmidt, C. Becher, O. Gühne, W. Dür, and R. Blatt, Scalable multiparticle entanglement of trapped ions, Nature (London) **438,** 643 (2005).

[32] J. Benhelm, G. Kirchmair, C. F. Roos, and R. Blatt, Towards fault-tolerant quantum computing with trapped ions, Nat. Phys. **4,** 463 (2008).

[33] K. Kim, M.-S. Chang, S. Korenblit, R. Islam, E. E. Edwards, J. K. Freericks, G.-D. Lin, L.-M. Duan, and C. Monroe, Quantum simulation of frustrated Ising spins with trapped ions, Nature (London) **465,** 590 (2010).

[34] B. P. Lanyon, C. Hempel, D. Nigg, M. Müller, R. Gerritsma, F. Zähringer, P. Schindler, J. T. Barreiro, M. Rambach, G. Kirchmair, M. Hennrich, P. Zoller, R. Blatt, and C. F. Roos, Universal digital quantum simulation with trapped ions, Science **334,** 57 (2011).

[35] R. Blatt and C. F. Roos, Quantum simulations with trapped ions, Nat. Phys. **8,** 277 (2012).

[36] J. W. Britton, B. C. Sawyer, A. C. Keith, C.-C. J. Wang, J. K. Freericks, H. Uys, M. J. Biercuk, and J. J. Bollinger, Engineered two-dimensional Ising interactions in a trapped-ion quantum simulator with hundreds of spins, Nature (London) **484,** 489 (2012).

[37] C. Kokail, C. Maier, R. van Bijnen, T. Brydges, M. K. Joshi, P. Jurcevic, C. A. Muschik, P. Silvi, R. Blatt, C. F. Roos, and P. Zoller, Self-verifying variational quantum simulation of lattice models, Nature (London) **569**, 355 (2019).

[38] J. M. Pino, J. M. Dreiling, C. Figgatt, J. P. Gaebler, S. A. Moses, M. S. Allman, C. H. Baldwin, M. Foss-Feig, D. Hayes, K. Mayer, C. Ryan-Anderson, and B. Neyenhuis, Demonstration of the trapped-ion quantum CCD computer architecture, Nature (London) **592**, 209 (2021).

[39] M. Ringbauer, M. Meth, L. Postler, R. Stricker, R. Blatt, P. Schindler, and T. Monz, A universal qudit quantum processor with trapped ions, Nat. Phys. **18**, 1053 (2022).

[40] W. Chen, Y. Lu, S. Zhang, K. Zhang, G. Huang, M. Qiao, X. Su, J. Zhang, J.-N. Zhang, L. Banchi, M. S. Kim, and K. Kim, Scalable and programmable phononic network with trapped ions, Nat. Phys. **19**, 877 (2023).

[41] O. Katz, L. Feng, A. Risinger, C. Monroe, and M. Cetina, Demonstration of three- and four-body interactions between trapped-ion spins, Nat. Phys. **19**, 1452 (2023).

[42] M. Qiao, Z. Cai, Y. Wang, B. Du, N. Jin, W. Chen, P. Wang, C. Luan, E. Gao, X. Sun, H. Tian, J. Zhang, and K. Kim, Tunable quantum simulation of spin models with a two-dimensional ion crystal, Nat. Phys. **20**, 623 (2024).

[43] S. C. Burd, R. Srinivas, J. J. Bollinger, A. C. Wilson, D. J. Wineland, D. Leibfried, D. H. Slichter, and D. T. C. Allcock, Quantum amplification of mechanical oscillator motion, Science **364**, 1163 (2019).

[44] K. C. McCormick, J. Keller, S. C. Burd, D. J. Wineland, A. C. Wilson, and D. Leibfried, Quantum-enhanced sensing of a single-ion mechanical oscillator, Nature (London) **572**, 86 (2019).

[45] K. A. Gilmore, M. Affolter, R. J. Lewis-Swan, D. Barberena, E. Jordan, A. M. Rey, and J. J. Bollinger, Quantum-enhanced sensing of displacements and electric fields with two-dimensional trapped-ion crystals, Science **373**, 673 (2021).

[46] D. Carney, H. Häffner, D. C. Moore, and J. M. Taylor, Trapped electrons and ions as particle detectors, Phys. Rev. Lett. **127**, 061804 (2021).

[47] D. Budker, P. W. Graham, H. Ramani, F. Schmidt-Kaler, C. Smorra, and S. Ulmer, Millicharged dark matter detection with ion traps, PRX Quantum **3**, 010330 (2021).

[48] T. Sailer, V. Debierre, Z. Harman, F. Heiße, C. König, J. Morgner, B. Tu, A. V. Volotka, C. H. Keitel, K. Blaum, and S. Sturm, Measurement of the bound-electron g-factor difference in coupled ions, Nature (London) **606**, 479 (2022).

[49] L. S. Brown and G. Gabrielse, Geonium theory: Physics of a single electron or ion in a Penning trap, Rev. Mod. Phys. **58**, 233 (1986).

[50] R. S. Van Dyck, P. B. Schwinberg, and H. G. Dehmelt, New high-precision comparison of electron and positron g factors, Phys. Rev. Lett. **59**, 26 (1987).

[51] S. Sturm, F. Köhler, J. Zatorski, A. Wagner, Z. Harman, G. Werth, W. Quint, C. H. Keitel, and K. Blaum, High-precision measurement of the atomic mass of the electron, Nature (London) **506**, 467 (2014).

[52] A. Cridland, J. H. Lacy, J. Pinder, and J. Verdú, Single microwave photon detection with a trapped electron, Photonics **3**, 59 (2016).

[53] D. L. Farnham, R. S. Van Dyck, and P. B. Schwinberg, Determination of the electron's atomic mass and the proton/electron mass ratio via Penning trap mass spectroscopy, Phys. Rev. Lett. **75**, 3598 (1995).

[54] S. Peil and G. Gabrielse, Observing the quantum limit of an electron cyclotron: QND measurements of quantum jumps between Fock states, Phys. Rev. Lett. **83**, 1287 (1999).

[55] R. K. Mittleman, I. I. Ioannou, H. G. Dehmelt, and N. Russell, Bound on *CPT* and Lorentz symmetry with a trapped electron, Phys. Rev. Lett. **83**, 2116 (1999).

[56] B. Odom, D. Hanneke, B. D'Urso, and G. Gabrielse, New measurement of the electron magnetic moment using a one-electron quantum cyclotron, Phys. Rev. Lett. **97**, 030801 (2006).

[57] D. Hanneke, S. Fogwell, and G. Gabrielse, New measurement of the electron magnetic moment and the fine structure constant, Phys. Rev. Lett. **100**, 120801 (2008).

[58] P. M. Platzman and M. I. Dykman, Quantum computing with electrons floating on liquid helium, Science **284**, 1967 (1999).

[59] G. Ciaramicoli, I. Marzoli, and P. Tombesi, Scalable quantum processor with trapped electrons, Phys. Rev. Lett. **91**, 017901 (2003).

[60] J. R. Zurita-Sánchez and C. Henkel, Wiring up single electron traps to perform quantum gates, New J. Phys. **10**, 083021 (2008).

[61] I. Marzoli, P. Tombesi, G. Ciaramicoli, G. Werth, P. Bushev, S. Stahl, F. Schmidt-Kaler, M. Hellwig, C. Henkel, G. Marx, I. Jex, E. Stachowska, G. Szawiola, and A. Walaszyk, Experimental and theoretical challenges for the trapped electron quantum computer, J. Phys. B **42**, 154010 (2009).

[62] D. I. Schuster, A. Fragner, M. I. Dykman, S. A. Lyon, and R. J. Schoelkopf, Proposal for manipulating and detecting spin and orbital states of trapped electrons on helium using cavity quantum electrodynamics, Phys. Rev. Lett. **105**, 040503 (2010).

[63] G. Yang, A. Fragner, G. Koolstra, L. Ocola, D. A. Czaplewski, R. J. Schoelkopf, and D. I. Schuster, Coupling an ensemble of electrons on superfluid helium to a superconducting circuit, Phys. Rev. X **6**, 011031 (2016).

[64] C. Matthiesen, Q. Yu, J. Guo, A. M. Alonso, and H. Häffner, Trapping electrons in a room-temperature microwave Paul trap, Phys. Rev. X **11**, 011019 (2021).

[65] A. Osada, K. Taniguchi, M. Shigefuji, and A. Noguchi, Feasibility study on ground-state cooling and single-phonon readout of trapped electrons using hybrid quantum systems, Phys. Rev. Res. **4**, 033245 (2022).

[66] R. T. Sutherland, Q. Yu, K. M. Beck, and H. Häffner, One- and two-qubit gate infidelities due to motional errors in trapped ions and electrons, Phys. Rev. A **105**, 022437 (2022).

[67] Q. Yu, A. M. Alonso, J. Caminiti, K. M. Beck, R. T. Sutherland, D. Leibfried, K. J. Rodriguez, M. Dhital, B. Hemmerling, and H. Häffner, Feasibility study of quantum computing using trapped electrons, Phys. Rev. A **105**, 022420 (2022).

[68] X. Zhou, G. Koolstra, X. Zhang, G. Yang, X. Han, B. Dizdar, X. Li, R. Divan, W. Guo, K. W. Murch, D. I. Schuster, and D. Jin, Single electrons on solid neon as a solid-state qubit platform, Nature (London) **605,** 46 (2022).

[69] E. Kawakami, J. Chen, M. Benito, and D. Konstantinov, Blueprint for quantum computing using electrons on helium, Phys. Rev. Appl. **20,** 054022 (2023).

[70] X. Zhou, X. Li, Q. Chen, G. Koolstra, G. Yang, B. Dizdar, Y. Huang, C. S. Wang, X. Han, X. Zhang, D. I. Schuster, and D. Jin, Electron charge qubit with 0.1 millisecond coherence time, Nat. Phys. **20,** 116 (2024).

[71] B. Yu, Y. Chu, R. Betzholz, S. Zhang, and J. Cai, Engineering artificial atomic systems of giant electric dipole moment, Phys. Rev. Lett. **132,** 073202 (2024).

[72] D. J. Wineland and W. M. Itano, Laser cooling of atoms, Phys. Rev. A **20,** 1521 (1979).

[73] D. An, A. M. Alonso, C. Matthiesen, and H. Häffner, Coupling two laser-cooled ions via a room-temperature conductor, Phys. Rev. Lett. **128,** 063201 (2022).

[74] M. Bohman, A. Mooser, G. Schneider, N. Schön, M. Wiesinger, J. Harrington, T. Higuchi, H. Nagahama, C. Smorra, S. Sellner, K. Blaum, Y. Matsuda, W. Quint, J. Walz, and S. Ulmer, Sympathetic cooling of protons and antiprotons with a common endcap Penning trap, J. Mod. Opt. **65,** 568 (2018).

[75] M. Bohman, *et al.*, Sympathetic cooling of a trapped proton mediated by an LC circuit, Nature (London) **596,** 514 (2021).

[76] C. Will, *et al.*, Sympathetic cooling schemes for separately trapped ions coupled via image currents, New J. Phys. **24,** 033021 (2021).

[77] C. Will, *et al.*, Image-current mediated sympathetic laser cooling of a single proton in a Penning trap down to 170 mK axial temperature, Phys. Rev. Lett. **133,** 023002 (2024).

[78] D. J. Heinzen and D. J. Wineland, Quantum-limited cooling and detection of radio-frequency oscillations by laser-cooled ions, Phys. Rev. A **42,** 2977 (1990).

[79] S. D. Fallek, V. S. Sandhu, R. A. McGill, J. M. Gray, H. N. Tinkey, C. R. Clark, and K. R. Brown, Rapid exchange cooling with trapped ions, Nat. Commun. **15,** 1089 (2024).

[80] B. Tu, F. Hahne, I. Arapoglou, A. Egl, F. Heiße, M. Höcker, C. König, J. Morgner, T. Sailer, A. Weigel, R. Wolf, and S. Sturm, Tank-circuit assisted coupling method for sympathetic laser cooling, Adv. Quantum Technol. **4,** 2100029 (2021).

[81] J. DiSciacca, M. Marshall, K. Marable, G. Gabrielse, S. Ettenauer, E. Tardiff, R. Kalra, D. W. Fitzakerley, M. C. George, E. A. Hessels, C. H. Storry, M. Weel, D. Grzonka, W. Oelert, and T. Sefzick (ATRAP Collaboration), One-particle measurement of the antiproton magnetic moment, Phys. Rev. Lett. **110,** 130801 (2013).

[82] A. Mooser, S. Ulmer, K. Blaum, K. Franke, H. Kracke, C. Leiteritz, W. Quint, C. C. Rodegheri, C. Smorra, and J. Walz, Direct high-precision measurement of the magnetic moment of the proton, Nature (London) **509,** 596 (2014).

[83] S. Ulmer, C. Smorra, A. Mooser, K. Franke, H. Nagahama, G. Schneider, T. Higuchi, S. Van Gorp, K. Blaum,

Y. Matsuda, W. Quint, J. Walz, and Y. Yamazaki, High-precision comparison of the antiproton-to-proton charge-to-mass ratio, Nature (London) **524,** 196 (2015).

[84] F. Heiße, F. Köhler-Langes, S. Rau, J. Hou, S. Junck, A. Kracke, A. Mooser, W. Quint, S. Ulmer, G. Werth, K. Blaum, and S. Sturm, High-precision measurement of the proton's atomic mass, Phys. Rev. Lett. **119,** 033001 (2017).

[85] C. Smorra, S. Sellner, M. J. Borchert, J. A. Harrington, T. Higuchi, H. Nagahama, T. Tanaka, A. Mooser, G. Schneider, M. Bohman, K. Blaum, Y. Matsuda, C. Ospelkaus, W. Quint, J. Walz, Y. Yamazaki, and S. Ulmer, A parts-per-billion measurement of the antiproton magnetic moment, Nature (London) **550,** 371 (2017).

[86] M. Niemann, T. Meiners, J. Mielke, M. J. Borchert, J. M. Cornejo, S. Ulmer, and C. Ospelkaus, Cryogenic $^9Be^+$ Penning trap for precision measurements with (anti-)protons, Meas. Sci. Technol. **31,** 035003 (2019).

[87] J. Tan and G. Gabrielse, Synchronization of parametrically pumped electron oscillators with phase bistability, Phys. Rev. Lett. **67,** 3090 (1991).

[88] M. Wittemer, F. Hakelberg, P. Kiefer, J.-P. Schröder, C. Fey, R. Schützhold, U. Warring, and T. Schaetz, Phonon pair creation by inflating quantum fluctuations in an ion trap, Phys. Rev. Lett. **123,** 180502 (2019).

[89] X. Fan, T. G. Myers, B. A. D. Sukra, and G. Gabrielse, Measurement of the electron magnetic moment, Phys. Rev. Lett. **130,** 071801 (2023).

[90] N. Daniilidis, T. Lee, R. Clark, S. Narayanan, and H. Häffner, Wiring up trapped ions to study aspects of quantum information, J. Phys. B **42,** 154012 (2009).

[91] D. J. Wineland and H. G. Dehmelt, Principles of the stored ion calorimeter, J. Appl. Phys. **46,** 919 (1975).

[92] L. S. Brown, Quantum motion in a Paul trap, Phys. Rev. Lett. **66,** 527 (1991).

[93] R. J. Glauber, in *Laser Manipulation of Atoms and Ions*, edited by E. Arimondo, W. D. Phillips, and F. Strumia, Proceedings of the International School of Physics "Enrico Fermi" Course 118 (North-Holland, Amsterdam, 1992), p. 643.

[94] D. Leibfried, R. Blatt, C. Monroe, and D. Wineland, Quantum dynamics of single trapped ions, Rev. Mod. Phys. **75,** 281 (2003).

[95] D. Kielpinski, D. Kafri, M. J. Woolley, G. J. Milburn, and J. M. Taylor, Quantum interface between an electrical circuit and a single atom, Phys. Rev. Lett. **108,** 130504 (2012).

[96] D. Kafri, P. Adhikari, and J. M. Taylor, Dynamics of an ion coupled to a parametric superconducting circuit, Phys. Rev. A **93,** 013412 (2016).

[97] F. W. J. Olver, A. B. O. Daalhuis, D. W. Lozier, B. I. Schneider, R. F. Boisvert, C. W. Clark, B. V. S. B. R. Mille and, H. S. Cohl, and M. A. McClain, eds., NIST digital library of mathematical functions, Release 1.1.12 of 2023-12-15, https://dlmf.nist.gov/.

[98] M. Abramowitz and I. A. Stegun, eds., *Handbook of Mathematical Functions: With Formulas, Graphs, and Mathematical Tables* (Dover Publications, New York, 1965).

[99] Z. Shu, Y. Liu, Q. Cao, P. Yang, S. Zhang, M. B. Plenio, F. Jelezko, and J. Cai, Observation of Floquet Raman transition in a driven solid-state spin system, Phys. Rev. Lett. **121,** 210501 (2018).

[100] R. Coïsson, G. Vernizzi, and X. Yang, in *2009 IEEE International Workshop on Open-source Software for Scientific Computation (OSSC)* (IEEE, Guiyang, 2009), p. 3.

[101] K. R. Brown, J. Kim, and C. Monroe, Co-designing a scalable quantum computer with trapped atomic ions, npj Quantum Inf. **2,** 1 (2016).

[102] J. P. Dowling, Quantum optical metrology—the lowdown on high-N00N states, Contemp. Phys. **49,** 125 (2008).

[103] A. Sørensen and K. Mølmer, Entanglement and quantum computation with ions in thermal motion, Phys. Rev. A **62,** 022311 (2000).

[104] C. F. Roos, Ion trap quantum gates with amplitude-modulated laser beams, New J. Phys. **10,** 013002 (2008).

[105] P. Paasche, C. Angelescu, S. Ananthamurthy, D. Biswas, T. Valenzuela, and G. Werth, Instabilities of an electron cloud in a Penning trap, Eur. Phys. J. D **22,** 183 (2003).

[106] K. T. Satyajit, A. Gupta, G. Joshi, S. Mohan, P. Rao, and S. Ananthamurthy, Loading detection and number estimation of an electron plasma in a Penning trap, Plasma Sci. Technol. **11,** 521 (2009).

[107] B. M. Dyavappa, D. Datar, Prakash, and S. Ananthamurthy, Dependence of the confinement time of an electron plasma on the magnetic field in a quadrupole Penning trap, EPJ Tech. Instrum. **4,** 1 (2017).

[108] D. A. Hite, Y. Colombe, A. C. Wilson, K. R. Brown, U. Warring, R. Jördens, J. D. Jost, K. S. McKay, D. P. Pappas, D. Leibfried, and D. J. Wineland, 100-fold reduction of electric-field noise in an ion trap cleaned with in situ argon-ion-beam bombardment, Phys. Rev. Lett. **109,** 103001 (2012).

[109] M. F. Brandl, M. W. van Mourik, L. Postler, A. Nolf, K. Lakhmanskiy, R. R. Paiva, S. Möller, N. Daniilidis, H. Häffner, V. Kaushal, T. Ruster, C. Warschburger, H. Kaufmann, U. G. Poschinger, F. Schmidt-Kaler, P. Schindler, T. Monz, and R. Blatt, Cryogenic setup for trapped ion quantum computing, Rev. Sci. Instrum. **87,** 113103 (2016).

[110] D. Kielpinski, C. Monroe, and D. J. Wineland, Architecture for a large-scale ion-trap quantum computer, Nature (London) **417,** 709 (2002).

[111] S. Olmschenk, D. N. Matsukevich, P. Maunz, D. Hayes, L.-M. Duan, and C. Monroe, Quantum teleportation between distant matter qubits, Science **323,** 486 (2009).

[112] L. J. Stephenson, D. P. Nadlinger, B. C. Nichol, S. An, P. Drmota, T. G. Ballance, K. Thirumalai, J. F. Goodwin, D. M. Lucas, and C. J. Ballance, High-rate, high-fidelity entanglement of qubits across an elementary quantum network, Phys. Rev. Lett. **124,** 110501 (2020).

[113] J. F. Goodwin, G. Stutter, R. C. Thompson, and D. M. Segal, Resolved-sideband laser cooling in a Penning trap, Phys. Rev. Lett. **116,** 143002 (2016).

[114] M. J. Borchert, P. E. Blessing, J. A. Devlin, J. A. Harrington, T. Higuchi, J. Morgner, C. Smorra, E. Wursten, M. Bohman, M. Wiesinger, A. Mooser, K. Blaum, Y. Matsuda, C. Ospelkaus, W. Quint, J. Walz, Y. Yamazaki, and S. Ulmer, Measurement of ultralow heating rates of a single antiproton in a cryogenic Penning trap, Phys. Rev. Lett. **122,** 043201 (2019).

[115] C. Rackauckas and Q. Nie, DifferentialEquations.jl—A performant and feature-rich ecosystem for solving differential equations in Julia, J. Open Res. Softw. **5,** 15 (2017).

[116] J. Sarnoff and JuliaMath, DoubleFloats, https://github.com/JuliaMath/DoubleFloats.jl (2022).

[117] W. Kaplan, *Advanced Calculus* (Addison-Wesley, Redwood City, 1991).